iScience

CellPress
OPEN ACCESS

Article

Ether-linked porphyrin covalent organic framework with broadband optical switch

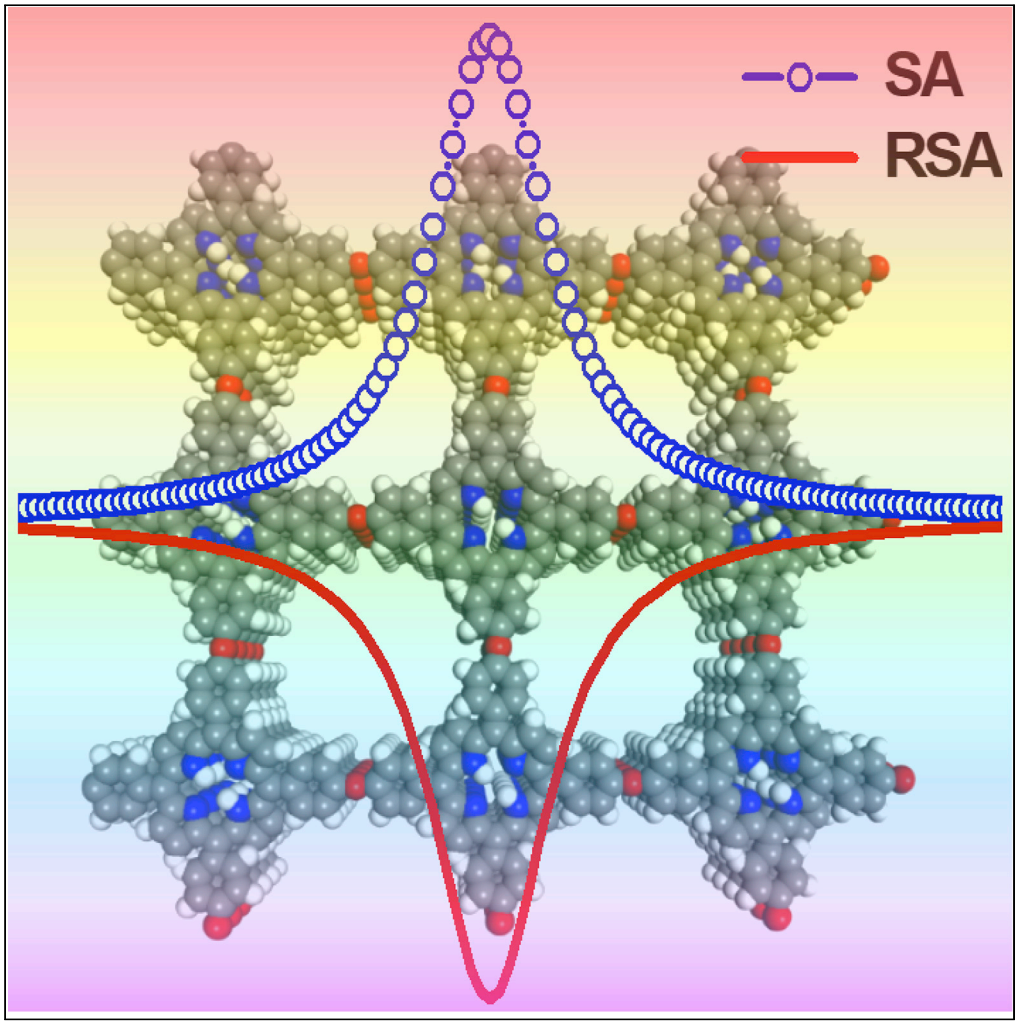

Zhiwei Liu, Bin Zhang, Yuelin Huang, Yi Song, Ningning Dong, Jun Wang, Yu Chen

amzhangbin@126.com (B.Z.)
chentangyu@yahoo.com (Y.C.)

Highlights

The first ether-linked porphyrin covalent organic framework (COF-Pors) was synthesized.

COF-Pors exhibits reversible intensity-dependent SA to RSA transition in DMF dispersions.

COF-Pors shows an NLO switching effect in a broad range from visible to near infrared.

COF-Pors exhibits SA at lower pulse energy and RSA at higher pulse energy.

Liu et al., iScience *24*, 102526
June 25, 2021
https://doi.org/10.1016/j.isci.2021.102526

iScience

CellPress
OPEN ACCESS

Article

Ether-linked porphyrin covalent organic framework with broadband optical switch

Zhiwei Liu,[1] Bin Zhang,[1,*] Yuelin Huang,[1,5] Yi Song,[3] Ningning Dong,[2,4] Jun Wang,[2,4] and Yu Chen[1,6,*]

SUMMARY

It is still a challenge to design and synthesize novel switchable optical materials with ultrafast nonlinear optical (NLO) response in a broad spectral range. These materials have exhibited great application potential in many high-technology fields such as biological imaging, chemical sensors, optical data storage, laser protection, and controllable intelligent and optoelectronic devices. By using porphyrins with highly delocalized 18 π-electron conjugated system as functional building blocks, the first ether-linked porphyrin covalent organic framework materials (COF-Pors) with highly ordered lattice structure have been successfully synthesized. In contrast to the starting porphyrins that only exhibit reverse saturable absorption (RSA) response at 532 nm, the as-prepared COF-Pors shows large NLO effect in a broad range from visible to near infrared. Upon laser illumination, COF-Pors exhibits typical saturable absorption (SA) effect at lower incident laser energy, and RSA response at higher pulse energy.

INTRODUCTION

As a unique and novel crystalline porous material with structural periodicity and inherent porosity of uniform topology, covalent organic frameworks (COFs) (Côté et al., 2005), which were for the first time successfully synthesized by Yaghi et al. through molecular building blocks in 2005, have received considerable attention and inspired numerous people's research enthusiasm due to their great application potential in gas storage and separation, drug delivery, smart sensors, molecular catalysis, energy storage, photonic and optoelectronic devices (Zeng et al., 2016; Ashraf et al., 2020; Sun et al., 2018; Ghazi et al., 2016; Bhunia et al., 2017; Keller et al., 2017; Dalapati et al., 2013; Peng et al., 2017; Biswal et al., 2019; Samal et al., 2019; Chen et al., 2019; Lu et al., 2019; Zhang et al., 2020; Quertinmont et al., 2020). In comparison with the three-dimensional (3D) COFs, the two-dimensional (2D) COFs are more promising because of two factors: (1) the degree of lateral conjugation from π orbitals present throughout the individual 2D layer and (2) the inherent π-π stacking between the two adjacent layers (Bhunia et al., 2017). To construct such COFs that have suitable geometry, good structural and environmental stability, and unique functional behaviors as well, one need to choose suitable linkers and/or linkages to connect the selected organic building blocks together (Geng et al., 2020; Kandambeth et al., 2019; Wang et al., 2019; Liang et al., 2020; Diercks et al., 2018; Keller et al., 2018; Shi et al., 2020; Li et al., 2019; Meng et al., 2020; Park et al., 2020; Feng et al., 2011, 2012; Wan et al., 2011; Lin et al., 2015; Liao et al., 2016; Huang et al., 2019; Guan et al., 2019). However, the linkers or linkages used for the realization of COF materials are mainly limited to the B=N, C–N, B–O, C=N and C=C bonds. No report concerns the ether-linked COFs so far.

Like phthalocyanines and fullerenes, porphyrins with the highly delocalized aromatic 18 π-electron system and the tremendous structural flexibility only exhibit reverse saturable absorption (RSA) effect at the visible region. Their nonlinear optical (NLO) absorption mechanism involves the population of excited states which absorb more effectively than the ground state. This gives rise to the phenomenon of RSA as a consequence of multiphoton absorption. It has been shown that porphyrin compounds exhibit RSA because of the occurrence of intersystem crossing from the lowest excited singlet state (S_1) to the lowest triplet state (T_1) and the subsequent increase in the population of the strongly absorbing T_1 state with nanosecond dynamics. To explore more potential applications of porphyrin-based functional materials, Yaghi et al. designed and synthesized two porphyrin-based crystalline COFs with high charge carrier mobilities, in which the porphyrin molecules were stacked laterally to produce an efficient conducting interface (Wan et al., 2011). Similarly, Jiang et al. also synthesized Zinc porphyrin-based COFs with a remarkable and positive size effect (Feng et al., 2011). Since then, a number of porphyrin-based COFs have been reported one after another in order to explore their potential applications in the high-technology fields (Lin et al., 2015; Liao et al., 2016; Huang et al., 2019; Guan et al., 2019). In

[1]Key Laboratory for Advanced Materials and Joint International Research Laboratory of Precision Chemistry and Molecular Engineering, Feringa Nobel Prize Scientist Joint Research Center, School of Chemistry and Molecular Engineering, East China University of Science and Technology, 130 Meilong Road, Shanghai 200237, China

[2]Laboratory of Micro-Nano Optoelectronic Materials and Devices, Key Laboratory of Materials for High-Power Laser, Shanghai Institute of Optics and Fine Mechanics, CAS, Shanghai 201800, China

[3]Department of Light Industry and Chemical Engineering, Guizhou Light Industry Technical College, 3 Dongqing Road, Huaxi University Town, Guiyang 550025, China

[4]State Department Key Laboratory of High Field Laser Physics Shanghai Institute of Optics and Fine Mechanics Chinese Academy of Sciences, Shanghai 201800, China

[5]School of Materials Science and Engineering, East China University of Science and Technology, 130 Meilong Road, Shanghai 200237, China

[6]Lead contact

*Correspondence: amzhangbin@126.com (B.Z.), chentangyu@yahoo.com (Y.C.)

https://doi.org/10.1016/j.isci.2021.102526

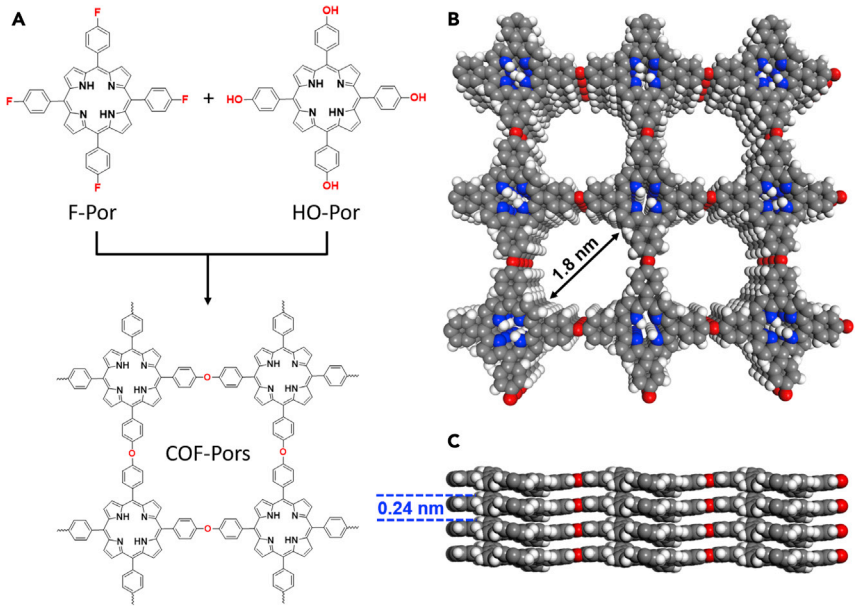

Figure 1. Synthesis and the packing models of COF-Pors

(A) Synthesis of COF-Pors.

(B) The packing model of COF-Pors indicating the pore aperture.

(C) The packing model indicating the π–π stacking distance between the individual layers.

this work, as shown in Figure 1, we designed and synthesized the first ether-linked porphyrin-based COFs (COF-Pors) with an interlayer distance of ~0.24 nm and a pore-size of ~1.8 nm. Similar to the representative 2D nanomaterial "g-C_3N_4" with the remarkable optoelectronic feature, the as-prepared COF-Pors has the almost same band structure as that of the former, suggesting the promising potential applications in photosynthesis, photonics and optoelectronics. Unlike the porphyrin molecules as the synthetic precursor, COF-Pors exhibited more excellent nonlinear optical (NLO) performance in a broad range from visible to near infrared. This work not only identified a suitable material candidate for the novel NLO optical switching devices but also paved the way for the construction of more ether-linked COFs in the near future.

RESULTS AND DISCUSSION

Crystallinity

The formation of the ether bond in COF-Pors can be easily achieved by a typical nucleophilic aromatic substitution reaction between Ar-F and Ar-OH. As shown in Figure S3, the Fourier transform infrared (FT-IR) spectrum of F-Por showed a weak absorption band of the C-F stretching mode at 1091 cm^{-1}, which disappeared in the IR spectrum of COF-Pors. HO-Por exhibited a strong broad absorption band in the region of 3200–3600 cm^{-1} due to the stretching vibration of the -OH groups. Similarly, F-Por and COF-Pors also showed weak absorption bands ($\nu_{\text{-NH}}$) in the same region. Also, the F1s signal observed in X-ray photoelectron spectroscopy (XPS) spectrum of F-Pors was not apparently detected in the XPS spectrum of COF-Pors (Figure S4). Furthermore, ^{13}C NMR signal assigned to carbon in C-O bonds of COF-Pors was observed in the solid-state ^{13}C CP-MAS NMR spectrum (Figure S2). These results suggested the successful formation of the ether bond in COF-Pors. Both the 2D-small angle X-ray scattering (SAXS) (Figure 2A) and powder X-ray diffraction (PXRD) (Figure 2B) patterns of COF-Pors demonstrated their crystalline nature. The experimentally observed XRD pattern of COF-Pors matched fairly well with the simulated ones derived from the eclipsed stacking (A-A stacking) models. Figure 2C showed a prominent bright diffraction ring (red solid line) at about 3.62 nm^{-1} (~0.28 nm), followed by a diffraction ring composed of some diffraction spots (yellow dashed line) at 4.25 nm^{-1} (~0.24 nm). This result suggested that there existed ordering cavity structure in COF-Pors (Zhang et al., 2018a, 2018b; Sahabudeen et al., 2016; Zhao et al., 2019). Furthermore, the multilayer feature of COF-Pors was observed at the edge of the COF-Pors film (Figure 2D). The SEM images showed a flake-like morphology (Figure S10). From Figures 2E and S8, it can be clearly seen that the COF-Pors film showed well-ordered structural feature due to the π-π stacking between the layers, from which the lattice finger distance was found to be about 0.24 nm (Figure 2E) and/or about 0.28 nm (Figure S8), which is in perfect consistent with the results from selected area

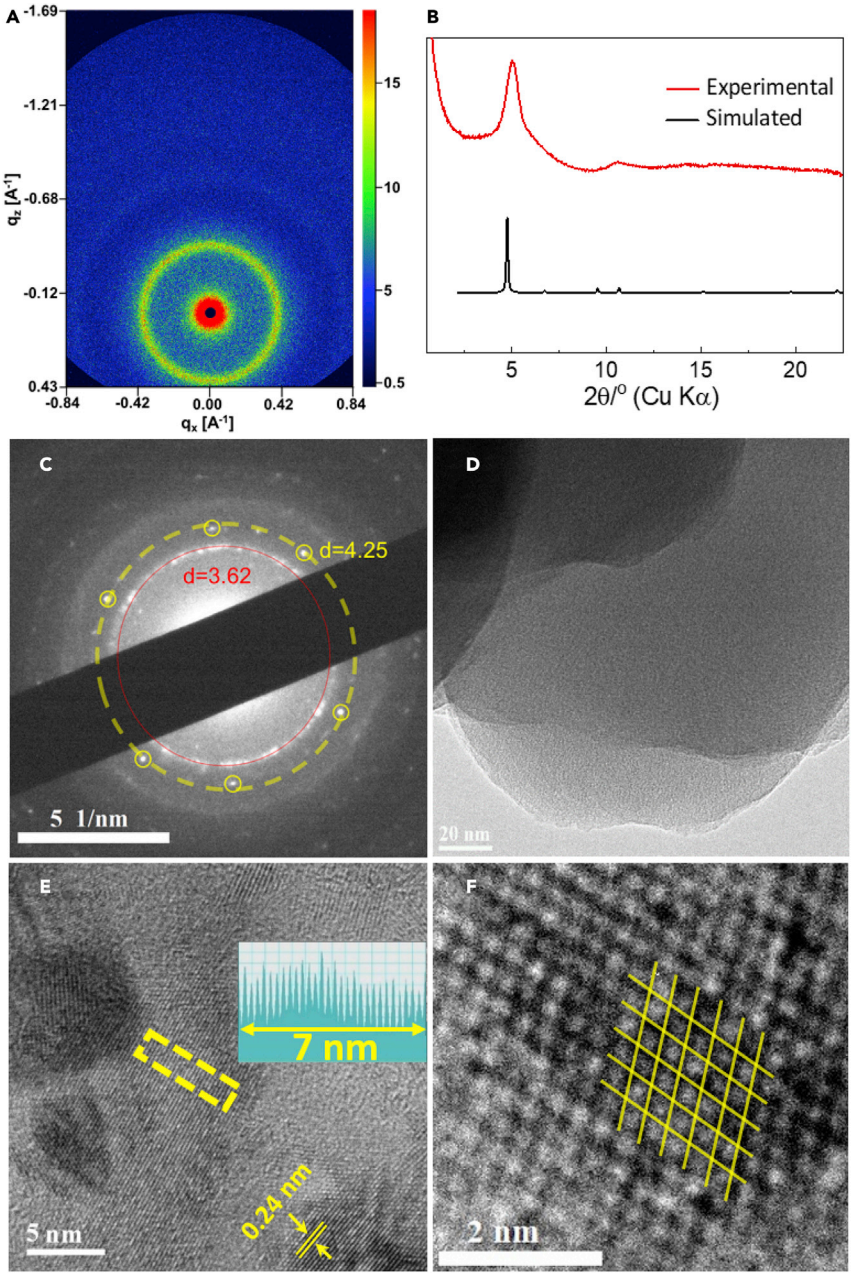

Figure 2. Crystallinity and TEM images of COF-Pors

(A) 2D small angle X-ray scattering (SAXS) of COF-Pors.

(B) Powder X-ray diffraction (PXRD) spectra of COF-Pors.

(C) Selected area electron diffraction (SAED) of COF-Pors.

(D–F) High resolution TEM images of COF-Pors. Inset in (E): the corresponding lattice distances.

electron diffraction. The 2D lattice image shown in Figure 2F revealed the highly ordered internal square-lattice structure of COF-Pors. The energy-dispersive X-ray analysis of COF-Pors demonstrated the uniform distribution of N, O, and C within the framework (Figure S9 and S11).

Porosity

By measuring the nitrogen adsorption isotherm at 77 K, one can determine the permanent porosity of COF-Pors. As shown in Figure S5, COF-Pors exhibited type I adsorption isotherms, indicating a microporous

character. The calculated BET surface area is about 101 $m^2 g^{-1}$. The relatively small surface area is possibly due to such a factor that the ether-bond linkers used for construction of COF-Pors lacks sufficient rigidity to prevent the network pores from blocking when compared with the traditional COF linkages with fixed configurations. The pore-size distribution analysis showed that a strong peak appeared at 1.8 nm, which is consistent with the theoretical value shown in Figure 1B.

Thermal stability and light-induced electronic behavior

From Figure S6, it can be seen that COF-Pors showed a good thermal stability. Its onset decomposition temperature (T_d) for the thermal bond cleavage is about 382°C in the air atmosphere, with a weight loss of 13.86 wt.% at this temperature. Figure S7 shows the electron paramagnetic resonance (EPR) spectra of COF-Pors before and under illumination. COF-Pors exhibited an EPR signal with a ΔH_{pp} (the peak-to-peak width) of 5.47 G and a *g* value of 2.0034 at room temperature. This signal may be associated with the existence of oxygen atoms in COF-Pors, which gives rise to the delocalization of π-electrons in such a larger aromatic system (Yu et al., 2021). Under illumination with a 532 nm laser, the observed EPR signal was apparently enhanced, with a *g* value of 2.0037 and a ΔH_{pp} of 5.67 G. This finding suggested the increase in concentration of the free radicals or unpaired electrons in the material system due to photoexcitation. Furthermore, the femtosecond transient absorption spectrum of COF-Pors in DMF (λ_{ex} = 400 nm) showed two main transient absorption bands at ~ 480 and 700 nm after the laser pulse irradiation (Figures S12A and S12B), suggesting the excited-state absorption in the material system. Like porphyrins and phthalocyanines, the enhanced EPR signal and the transient absorption bands can be assigned to the strong excited-state absorption of COF-Pors under laser illumination (Sanghadasa et al., 2001; Chen et al., 2005). From the time profile of the excited-state absorption band at 700 nm, the excited-state lifetime of COF-Pors is estimated as about 460 ps (Figure S12C). Moreover, both the spatial charge-carrier transport channels formed by the eclipsed stacking and the planar-extended π-conjugation effect (Feng et al., 2012) can result in an increase in the excited-state absorption cross section of COF-Pors, and thereby improving the NLO performance of COF-Pors.

Electronic absorption and HOMO/LUMO energy levels

To gain a deeper insight into the optical and electronic structure properties of COF-Pors, we carried out the ultraviolet photoelectron spectroscopy (UPS) and ultraviolet-visible (UV-Vis) absorption spectral experiments. The UV-Vis absorption spectra of COF-Pors and its two synthetic precursors "F-Por and HO-Por" are almost similar, with an intense B-band at 410~430 nm and the Q bands in 500-700 nm region (Figure 3A). The B-bands of F-Por and HO-Por were located at 415 nm and 422 nm, respectively, while the B-band of COF-Pors appeared at 430 nm due to the planar extended π-conjugation effect. From the Tauc plot shown in Figure 3B, one can easily estimate the optical bandgap ($Eg^{opt.}$) of COF-Pors (~2.79 eV). This implies that like *g*-C_3N_4 with a $Eg^{opt.}$ of ~2.7 eV (Wang et al., 2009), COF-Pors also exhibit an intrinsic semiconductor-like absorption in the blue region of the electronic absorption spectrum. According to the method reported in literature (Zhang et al., 2018a, 2018b; Liu et al., 2016), the HOMO energy level of COF-Pors was calculated as −6.02 eV from the UPS spectrum (Figure 3C). By using the equation, $E_{LUMO} = E_{HOMO} + Eg^{opt.}$, the LUMO level of COF-Pors can be achieved. As a result, its LUMO energy level is −3.23 eV. These values can be converted to the corresponding electrochemical potentials according to the reference standard for which 0 V vs. reversible hydrogen electrode equals −4.44 eV vs. vacuum level (Liu et al., 2015). From Figure 3D, one can see that both the reduction level of H_2 and the reduction potential of CO/CO_2 are positioned below the LUMO level of COF-Pors, whereas the oxidation level for H_2O to O_2 is located above the HOMO level of COF-Pors. And more, the HOMO/LUMO energy levels of COF-Pors are found to be quite similar to these of *g*-C_3N_4 (HOMO: −5.95 eV; LUMO: −3.25 eV). These results suggested that COF-Pors would have great application potential in photosynthesis, photocatalysis, and optoelectronics.

Nonlinear optical response

As a proof-of concept application, we used nanosecond Z-scan technique, which can measure the total transmittance through the sample as a function of incident laser intensity while the sample is gradually moved through the focus point of a lens along the z axis, to explore the nonlinear optical switching effect of COF-Pors in a broad range from the visible to the near infrared. Figures 4A and 4B showed the excitation pulse energy dependent Z-scan data of COF-Pors dispersed in DMF at both 532 and 1064 nm. The normalized transmittance (T_{min}) curves of COF-Pors in DMF showed a symmetrical peak onto the laser focal point (z = 0), with a maximum response of ~18.4% at 532 nm and ~12.6% at 1064 nm at the lowest excitation of 40μJ. This suggested a saturable absorption (SA) performance. When the incident laser energy was larger than 70μJ at 532 nm or 150μJ at 1064 nm, the RSA became dominant, while SA became negligible. This intensity-dependent

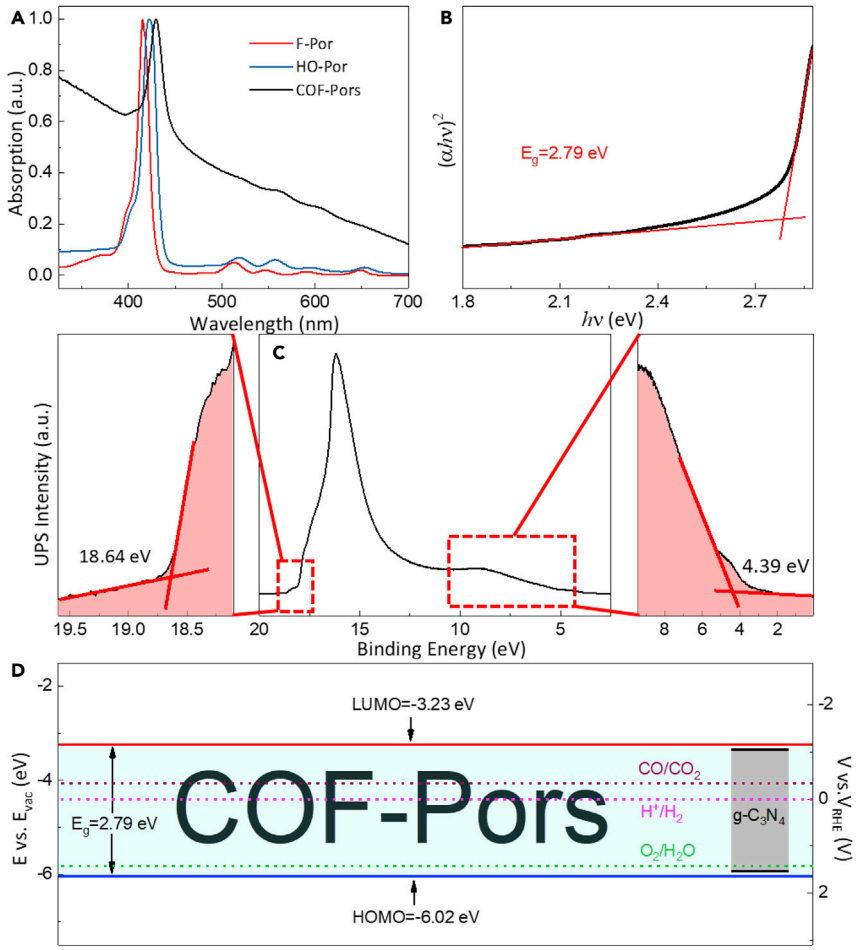

Figure 3. Electronic absorption and HOMO/LUMO energy levels of COF-Pors

(A) UV-Vis absorption spectra of the samples in DMF.

(B) $(\alpha h\nu)^2$ vs. $h\nu$ curve of COF-Pors, this curve is also called as the Tauc plot.

(C) UPS spectrum of COF-Pors.

(D) HOMO/LUMO energy levels of COF-Pors.

SA to RSA transition was found to be perfectly reversible in DMF. Similarly, the polymer-covalently functionalized 2D MoS_2 nanosheets (Shi et al., 2017; Cheng et al., 2016) also exhibited the transition from SA to RSA at higher incident pulse energy. At high incident energy regime at 532 nm, the T_{min} value gradually decreased with the increasing of incident pulse laser energy: 0.83 at 100μJ → 0.64 at 300μJ. In contrast to the observation at 532 nm, the transmittance curve exhibited a valley within the peak at the focus at 1064 nm due to the thermally induced nonlinear scattering effect that occurs following SA. The observed lowest T_{min} reached to 0.83 at 300μJ at 1064 nm. From Figures 4C and 4D, it can be seen that COF-Pors displayed excellent NLO performance at both 532 and 1064 nm when compared to their synthetic precursors F-Por and HO-Por. As expected, both the F-Por and HO-Por only showed typical RSA response at 532 nm. No any NLO response was observed at 1064 nm. These findings demonstrated that the as-prepared COF-Pors exhibited broadband nonlinear switching and optical limiting (OL) performance. The photon energy of the 532 nm laser is about 2.33 eV, which is smaller than the bandgap of COF-Pors (~2.79 eV). At low incident energy regime, the energy of the incident photon is not large enough to excite the electrons of COF-Pors from the ground state to the excited state. In this case, COF-Pors will undergo the ground state bleaching process, leading to a typical SA response. With the increase of laser energy, the number of photons increases rapidly. At this time, electrons of COF-Pors in the ground state will absorb more photons and be excited to the excited state, giving rise to a multi-photon absorption-induced RSA response. With increasing the incident laser energy, the excited-state absorption of COF-Pors will become dominant and consequently the T_{min} value will be considerably decreased. In contrast to the 532 nm laser, the photon energy of the 1064 nm is only about 1.17 eV, much smaller than the bandgap of

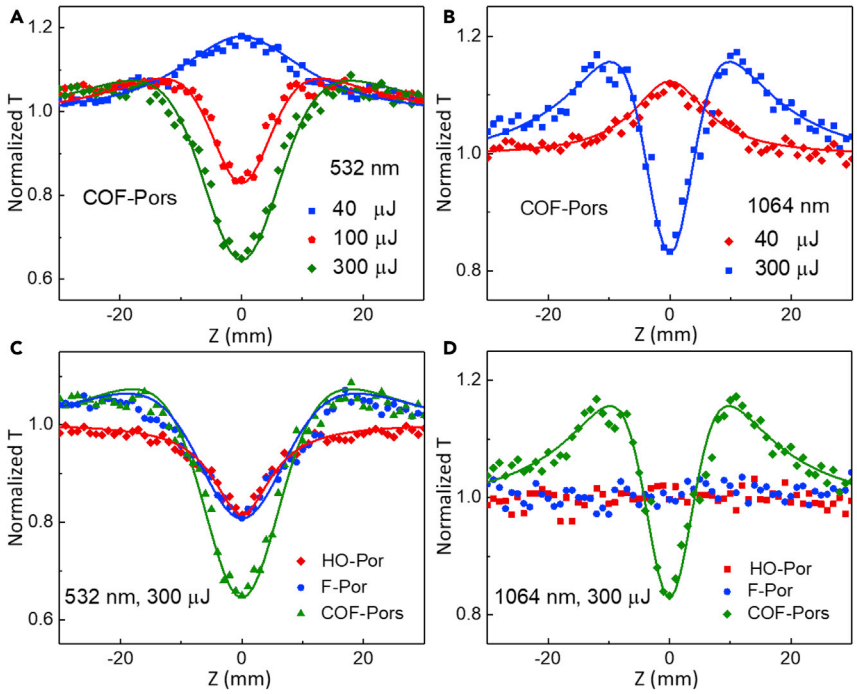

Figure 4. Nonlinear optical properties of COF-Pors

Typical open-aperture Z-scan data with normalized transmittance as a function of the sample position Z for samples dispersed in DMF under the excitation of 6 ns pulses at λ = 532 nm (A and C) and 1064 nm (B and D) with different energies. The solid lines are the theoretical fitting results. A repetition frequency used in this work is 10 Hz.

COF-Pors (~2.79 eV). And more, the wavelength of the incident laser at 1064 nm has been beyond the response region of the excited-state absorption. Similar to the graphene dispersions in organic solvents, the COF-Pors dispersed in DMF also showed strong NLO response due to the thermally induced nonlinear scattering (NLS) effect at 1064 nm. The induced scattering centers mainly included (1) the formation and growth of solvent bubbles, which is due to the thermal energy transfer from the COF-Pors to the DMF solvent; and (2) the formation and expansion of microplasmas as a result of the ionization of COF-Pors (Chen et al., 2016). The thermodynamical properties of DMF make a considerable contribution to the NLO and OL performance of COF-Pors dispersions at 1064 nm.

Conclusion

We have designed and synthesized the first ether-linked porphyrin COF materials with large NLO response in a broad range from visible to near infrared. The observed reversible intensity-dependent SA to RSA transition would be expected to find potential applications in all-optical intensity-dependent logic gates, and photonics, optoelectronics, photosynthesis, and photocatalysis in the future. The major ongoing areas of effort should be focused on the design and synthesis of new porphyrin/phthalocyanine-based COF materials for broadband switchable optical devices.

Limitations of the study

This work is mainly focused on the design and synthesis of the first ether-linked porphyrin-based COF material. Its nonlinear optical and OL properties were only briefly investigated by using open-aperture Z-scan system. In order to connect the fundamental studies to the industrial applications, one would concentrate on the solid state nonlinear optical materials. The future work should be focused on the design of new high-performance nonlinear optical materials and determination of the relationship between the structural parameters and the nonlinear optical switching response while seeking to optimally combine materials and devices.

STAR★METHODS

Detailed methods are provided in the online version of this paper and include the following:

SUPPLEMENTAL INFORMATION

Supplemental information can be found online at https://doi.org/10.1016/j.isci.2021.102526.

ACKNOWLEDGMENTS

This work is supported by the National Natural Science Foundation of China (61378072, 61178007, 61522510, and 61308087), Joint project of Ministry of Education and State Administration of Foreign Experts Affairs (TS2010HDLG024), the Strategic Priority Research Program of CAS (XDB160307), the Key Research Program of Frontier Science of CAS (QYZDB-SSW-JSC041), the STCSM Excellent Academic Leader of Shanghai (No. 17XD1403900). The authors also thank Kang Yan from the Research Center of Analysis and Test of East China University of Science and Technology for the structural characterization of materials.

AUTHOR CONTRIBUTIONS

Y.C., Z.L. and B.Z. conceived the idea. Z.L., Y.H. and Y.S. synthesized and characterized COF-Pors; N.D. and J.W. measured the NLO performance of COF-Pors; Y.C. wrote the manuscripts. All authors discussed the experimental results.

DECLARATION OF INTERESTS

The authors declare no competing interests.

Received: February 22, 2021
Revised: April 10, 2021
Accepted: May 7, 2021
Published: June 25, 2021

REFERENCES

Ashraf, S., Liu, C., Li, S., Haq, I.U., Mehmood, M., Li, P., and Wang, B. (2020). Versatile platform of ion conducting 2D anionic germanate covalent organic frameworks with potential for capturing toxic acidic gases. ACS Appl. Mater. Inter. *12*, 40372–40380.

Bhunia, S., Das, S.K., Jana, R., Peter, S.C., Bhattacharya, S., Addicoat, M., Bhaumik, A., and Pradhan, A. (2017). Electrochemical stimuli-driven facile metal-free hydrogen evolution from pyrene-porphyrin-based crystalline covalent organic framework. ACS Appl. Mater. Inter. *9*, 23843–23851.

Biswal, B.P., Valligatla, S., Wang, M., Banerjee, T., Saad, N.A., Mariserla, B.M.K., Chandrasekhar, N., Becker, D., Addicoat, M., Senkovska, I., et al. (2019). Nonlinear optical switching in regioregular porphyrin covalent organic frameworks. Angew. Chem. Int. Ed. *58*, 6896–6900.

Chen, Y., Hanack, M., Araki, Y., and Ito, O. (2005). Axially modified gallium phthalocyanines and naphthalocyanines for optical limiting. Chem. Soc. Rev. *34*, 517–529.

Chen, Y., Bai, T., Dong, N., Fan, F., Zhang, S., Zhuang, X., Sun, J., Zhang, B., Zhang, X., Wang, J., et al. (2016). Graphene and its derivatives for laser protection. Prog. Mater. Sci. *84*, 118–157.

Chen, R., Shi, J.L., Ma, Y., Lin, G., Lang, X., and Wang, C. (2019). Designed synthesis of a 2D porphyrin-based sp^2 carbon-conjugated covalent organic framework for heterogeneous photocatalysis. Angew. Chem. Int. Ed. *58*, 6430–6434.

Cheng, H., Dong, N., Bai, T., Song, Y., Wang, J., Qin, Y., Zhang, B., and Chen, Y. (2016). Covalent modification of MoS_2 with poly(N-vinylcarbazole) for solid-state broadband optical limiters. Chem. Eur. J. *22*, 4500–4507.

Côté, A.P., Benin, A.I., Ockwig, N.W., O'Keeffe, M., Matzger, A.J., and Yaghi, O.M. (2005). Porous, crystalline, covalent organic frameworks. Science *310*, 1166–1170.

Dalapati, S., Jin, S., Gao, J., Xu, Y., Nagai, A., and Jiang, D. (2013). An azine-linked covalent organic framework. J. Am. Chem. Soc. *135*, 17310–17313.

Diercks, C.S., Lin, S., Kornienko, N., Kapustin, E.A., Nichols, E.M., Zhu, C., Zhao, Y., Chang, C.J., and Yaghi, O.M. (2018). Reticular electronic tuning of porphyrin active sites in covalent organic frameworks for electrocatalytic carbon dioxide reduction. J. Am. Chem. Soc. *140*, 1116–1122.

Feng, X., Chen, L., Dong, Y., and Jiang, D. (2011). Porphyrin-based two-dimensional covalent organic frameworks: synchronized synthetic control of macroscopic structures and pore parameters. Chem. Commun. *47*, 1979–1981.

Feng, X., Liu, L., Honsho, Y., Saeki, A., Seki, S., Irle, S., Dong, Y., Nagai, A., and Jiang, D. (2012). High-rate charge-carrier transport in porphyrin covalent organic frameworks: switching from hole to electron to ambipolar conduction. Angew. Chem. Int. Ed. *51*, 2618–2622.

Geng, K., He, T., Liu, R., Dalapati, S., Tan, K.T., Li, Z., Tao, S., Gong, Y., Jiang, Q., and Jiang, D. (2020). Covalent organic frameworks: design, synthesis, and functions. Chem. Rev. *120*, 8814–8933.

Ghazi, Z.A., Zhu, L., Wang, H., Naeem, A., Khattak, A.M., Liang, B., Khan, N.A., Wei, Z., Li, L., and Tang, Z. (2016). Efficient polysulfide chemisorption in covalent organic frameworks for high-performance lithium-sulfur batteries. Adv. Energy Mater. *6*, 1601250.

Guan, X., Li, H., Ma, Y., Xue, M., Fang, Q., Yan, Y., Valtchev, V., and Qiu, S. (2019). Chemically stable polyarylether-based covalent organic frameworks. Nat. Chem. *11*, 587–594.

Huang, H., Li, F., Zhang, Y., and Chen, Y. (2019). Two-dimensional graphdiyne analogue Co-coordinated porphyrin covalent organic framework nanosheets as a stable electrocatalyst for the oxygen evolution reaction. J. Mater. Chem. A *7*, 5575–5582.

Kandambeth, S., Dey, K., and Banerjee, R. (2019). Covalent organic frameworks: chemistry beyond the structure. J. Am. Chem. Soc. *141*, 1807–1822.

Keller, N., Bessinger, D., Reuter, S., Calik, M., Ascherl, L., Hanusch, F.C., Auras, F., and Bein, T. (2017). Oligothiophene-bridged conjugated covalent organic frameworks. J. Am. Chem. Soc. *139*, 8194–8199.

Keller, N., Calik, M., Sharapa, D., Soni, H.R., Zehetmaier, P.M., Rager, S., Auras, F., Jakowetz, A.C., Gorling, A., Clark, T., et al. (2018). Enforcing extended porphyrin J-aggregate stacking in covalent organic frameworks. J. Am. Chem. Soc. *140*, 16544–16552.

Li, B.Q., Zhang, S.Y., Chen, X., Chen, C.Y., Xia, Z.J., and Zhang, Q. (2019). One-pot synthesis of framework porphyrin materials and their applications in bifunctional oxygen electrocatalysis. Adv. Funct. Mater. *29*, 1901301.

Liang, R.R., Jiang, S.Y., Ru-Han, A., and Zhao, X. (2020). Two-dimensional covalent organic frameworks with hierarchical porosity. Chem. Soc. Rev. *49*, 3920–3951.

Liao, H., Wang, H., Ding, H., Meng, X., Xu, H., Wang, B., Ai, X., and Wang, C. (2016). A 2D porous porphyrin-based covalent organic framework for sulfur storage in lithium–sulfur batteries. J. Mater. Chem. A *4*, 7416–7421.

Lin, S., Diercks, C.S., Zhang, Y., Kornienko, N., Nichols, E.M., Zhao, Y., Paris, A.R., Kim, D., Yang, P., Yaghi, O.M., et al. (2015). Covalent organic frameworks comprising cobalt porphyrins for catalytic CO2 reduction in water. Science *349*, 1208–1213.

Liu, J., Liu, Y., Liu, N., Han, Y., Zhang, X., Huang, H., Lifshitz, Y., Lee, S.T., Zhong, J., and Kang, Z. (2015). Water splitting. Metal-free efficient photocatalyst for stable visible water splitting via a two-electron pathway. Science *347*, 970–974.

Liu, Y., Hong, Z., Chen, Q., Chen, H., Chang, W.H., Yang, Y.M., Song, T.B., and Yang, Y. (2016). Perovskite solar cells employing dopant-free organic hole transport materials with tunable energy levels. Adv. Mater. *28*, 440–446.

Lu, M., Liu, J., Li, Q., Zhang, M., Liu, M., Wang, J.L., Yuan, D.Q., and Lan, Y.Q. (2019). Rational design of crystalline covalent organic frameworks for efficient CO2 photoreduction with H2O. Angew. Chem. Int. Ed. *58*, 12392–12397.

Meng, Y., Luo, Y., Shi, J.L., Ding, H., Lang, X., Chen, W., Zheng, A., Sun, J., and Wang, C. (2020). 2D and 3D porphyrinic covalent organic frameworks: the influence of dimensionality on functionality. Angew. Chem. Int. Ed. *59*, 3624–3629.

Park, S., Liao, Z., Ibarlucea, B., Qi, H., Lin, H., Becker, D., Melidonie, J., Zhang, T., Sahabudeen, H., Baraban, L., et al. (2020). Two-dimensional boronate ester covalent organic framework thin films with large single crystalline domains for a neuromorphic memory device. Angew. Chem. Int. Ed. *59*, 8218–8224.

Peng, Y., Huang, Y., Zhu, Y., Chen, B., Wang, L., Lai, Z., Zhang, Z., Zhao, M., Tan, C., Yang, N., et al. (2017). Ultrathin two-dimensional covalent organic framework nanosheets: preparation and application in highly sensitive and selective DNA detection. J. Am. Chem. Soc. *139*, 8698–8704.

Qin, Y., Guo, H., Sheng, X., Wang, X., and Wang, F. (2015). An aluminum porphyrin complex with high activity and selectivity for cyclic carbonate synthesis. Green. Chem. *17*, 2853–2858.

Quertinmont, J., Maschio, L., Datta, A., and Champagne, B. (2020). J. Phys. Chem. C *124*, 24451–24459.

Sahabudeen, H., Qi, H., Glatz, B.A., Tranca, D., Dong, R., Hou, Y., Zhang, T., Kuttner, C., Lehnert, T., Seifert, G., et al. (2016). Wafer-sized multifunctional polyimine-based two-dimensional conjugated polymers with high mechanical stiffness. Nat. Commun. *7*, 13461.

Samal, M., Valligatla, S., Saad, N.A., Rao, M.V., Rao, D.N., Sahu, R., and Biswal, B.P. (2019). A thiazolo[5,4-d]thiazole-bridged porphyrin organic framework as a promising nonlinear optical material. Chem. Commun. *55*, 11025–11028.

Sanghadasa, M., Shin, I.-S., Clark, R.D., Guo, H., and Penn, B.G. (2001). Optical limiting behavior of octa-decyloxy metallo-phthalocyanines. J. Appl. Phys. *90*, 31–37.

Shi, M., Dong, N., He, N., Wan, Y., Cheng, H., Han, M., Wang, J., and Chen, Y. (2017). MoS2 nanosheets covalently functionalized with polyacrylonitrile: synthesis and broadband laser protection performance. J. Mater. Chem. C *5*, 11920–11926.

Shi, J.L., Chen, R., Hao, H., Wang, C., and Lang, X. (2020). 2D sp^2 carbon-conjugated porphyrin covalent organic framework for cooperative photocatalysis with TEMPO. Angew. Chem. Int. Ed. *59*, 9088–9093.

Sun, J., Klechikov, A., Moise, C., Prodana, M., Enachescu, M., and Talyzin, A.V. (2018). A molecular pillar approach to grow vertical covalent organic framework nanosheets on graphene: hybrid materials for energy storage. Angew. Chem. Int. Ed. *57*, 1034–1038.

Wan, S., Gándara, F., Asano, A., Furukawa, H., Saeki, A., Dey, S.K., Liao, L., Ambrogio, M.W., Botros, Y.Y., Duan, X., et al. (2011). Covalent organic frameworks with high charge carrier mobility. Chem. Mater. *23*, 4094–4097.

Wang, X., Maeda, K., Thomas, A., Takanabe, K., Xin, G., Carlsson, J.M., Domen, K., and Antonietti, M. (2009). A metal-free polymeric photocatalyst for hydrogen production from water under visible light. Nat. Mater. *8*, 76–80.

Wang, H., Zeng, Z., Xu, P., Li, L., Zeng, G., Xiao, R., Tang, Z., Huang, D., Tang, L., Lai, C., et al. (2019). Recent progress in covalent organic framework thin films: fabrications, applications and perspectives. Chem. Soc. Rev. *48*, 488–516.

Yu, Z., Wang, L., Mu, X., Chen, C., Wu, Y., Cao, J., and Tang, Y. (2021). Intramolecular electric field construction in metal phthalocyanine as dopant-free hole transporting material for stable perovskite solar cells with >21 % efficiency. Angew. Chem. Int. Ed. *60*, 6294–6299.

Zeng, Y., Zou, R., and Zhao, Y. (2016). Covalent organic frameworks for CO2 capture. Adv. Mater. *28*, 2855–2873.

Zhang, B., Wei, M., Mao, H., Pei, X., Alshmimri, S.A., Reimer, J.A., and Yaghi, O.M. (2018a). Crystalline dioxin-linked covalent organic frameworks from irreversible reactions. J. Am. Chem. Soc. *140*, 12715–12719.

Zhang, T., Hou, Y., Dzhagan, V., Liao, Z., Chai, G., Loffler, M., Olianas, D., Milani, A., Xu, S., Tommasini, M., et al. (2018b). Copper-surface-mediated synthesis of acetylenic carbon-rich nanofibers for active metal-free photocathodes. Nat. Commun. *9*, 1140.

Zhang, L., Zhou, Y., Jia, M., He, Y., Hu, W., Liu, Q., Li, J., Wang, C., Carlsson, A., Lazar, S., et al. (2020). Covalent organic framework for efficient two-photon absorption. Matter *2*, 1049–1063.

Zhao, Y., Liu, H., Wu, C., Zhang, Z., Pan, Q., Hu, F., Wang, R., Li, P., Huang, X., and Li, Z. (2019). Fully conjugated two-dimensional sp^2-carbon covalent organic frameworks as artificial photosystem I with high efficiency. Angew. Chem. Int. Ed. *58*, 5376–5381.

STAR★METHODS

KEY RESOURCES TABLE

REAGENT or RESOURCE	SOURCE	IDENTIFIER
Chemicals		
5,10,15,20-Tetrakis(4-hydroxyphenyl) porphyrin (HO-Por) (>95.0%)	Aladdin	CAS: 51094-17-8
Potassium carbonate (K_2CO_3) (GR, 99.5%)	Aladdin	CAS: 584-08-7
1,3,5-trimethyl- benzene (≥98.0%, H_2O≤ 50ppm)	Aladdin	CAS: 108-67-8
N-Methylpyrrolidone (NMP) (GC, >99.5%)	Aladdin	CAS: 872-50-4
N,N-Dimethylformamide (DMF) (AR, 99.5%)	Aladdin	CAS: 68-12-2
Tetrahydrofuran (THF) (AR, 99.0%)	Aladdin	CAS: 109-99-9

RESOURCE AVAILABILITY

Lead contact

Further information and requests for resources and reagents should be directed to and will be fulfilled by the lead contact, Prof. Yu Chen (chentangyu@yahoo.com).

Material availability

This study did not generate new unique reagents.

Data and code availability

This study did not generate data sets/code.

METHOD DETAILS

All the analytically pure chemicals were purchased from Aladdin and used without further purification. Organic solvents were purified, dried, and distilled under dry nitrogen. HO-Por was purchased from Aladdin and F-Por was synthesized according to the literature (Qin et al., 2015). The detailed information about the synthetic procedure, measurements, instruments and structural modeling are listed as follows.

Measurements and instruments

The ultraviolet visible (UV-Vis) absorption spectra were recorded on a Shimadzu UV-2600 spectrophotometer. Fourier transform infrared (FT-IR) spectra were performed on a Nicolet Nagma-IR 550 spectrophotometer using KBr pellets. Transmission electron microscopy (TEM) images were obtained using a JEOL-2100 (JEOL Ltd., Japan) TEM system operated at 200 kV. X-ray photoelectron spectroscopy (XPS) was carried out on a Kratos AXIS HSi spectrometer with a monochromatized Al KR X-ray source (1486.6 eV photons) at a constant dwell time of 100 ms and a pass energy of 40 eV. A Bruker ELEXSYS 100G-18KG/EMX-8/2.7C spectrometer in conjunction with a split-coil 6T superconducting magnet was used for W-band (95 GHz) electron paramagnetic resonance (EPR). X-ray diffraction (XRD) patterns were recorded on D/max 2500pc (Rigaku) for Cu Kα radiation (1.5406 Å). Nitrogen physisorption measurements were performed at 77 K, maintained by a liquid nitrogen bath, using ASAP2460 instrument (Micromeritics). SEM measurements were executed with a Hitachi S-3400N instrument. Ultraviolet Photoelectron Spectrometer (UPS) spectrum was recorded on an Escalab 250Xi (Thermo Scientific). MALDI-TOF-MS was collected on an Ionization Time of Flight Mass Spectrometry with Matrix-Assisted Laser Desorption (ABS, Singapore). ^{13}C CP solid-state NMR spectrum was recorded on an Agilent 600MHz instrument. The Femtosecond transient absorption (fs-TA) spectra were recorded on an HELIOS Fire Femtosecond Transient Absorption Spectrometer (Ultrafast System, USA) with the λ_{ex}=400 nm in NMP. PXRD data were obtained by small angle X-ray scattering (SAXS) using Xeuss 2.0 (Xenocs) with the detector Pilatus 300K. The sample-detector distance and beam center were calibrated using Silver Behenate. The 1-D line profile is obtained by converting the SAXS data to 2θ values, assuming λ = 1.5406 Å (Cu Kα). Thermogravimetric analyses (TGA) were carried out on a TGA8000 (PerkinElmer) in both N_2 and air. The NLO and OL properties of the sample dispersed in

DMF were studied through a typical open-aperture Z-scan system which has been widely used to investigate the NLO responses of materials. The measurements were performed using 6 ns pulses from a Q-switched Nd:YAG laser operating at 1064 nm and its second harmonic at λ=532 nm. The laser beam was tightly focused with a 15 cm focus lens. All dispersions were tested in 10×1 mm quartz cuvettes with the pulse repetition rate of 10 Hz.

Synthetic procedure

Synthesis of COF-Pors: A mixture of F-Por (103 mg, 0.15 mmol), HO-Por (67.8 mg, 0.1 mmol), and anhydrous K_2CO_3 (138.2 mg, 1.0 mmol) in mixed solvents of 1,3,5-trimethyl- benzene (1mL) and NMP (2mL) was sonicated for 15 minutes in order to get a homogenous dispersion. After that, the reaction mixture was then flash frozen at 77 K (in a liquid N_2 bath) and degassed by three freeze-pump-thaw cycles, followed by sealing under vacuum. After warming to room temperature, the mixture was heated at 130 oC and left undisturbed for 10 days. A black precipitate was isolated by filtration through a filter paper with an aperture of 0.25 μm and washed with DMF (50 mL). The solid was successively immersed in DMF (200 mL), water (200 mL), THF (200 mL) and acetone (200 mL) at 50 °C each for 3 d, during which the solvent was decanted and replaced 4 times per day. Finally, the precipitate was freeze-dried for 24 h and then evacuated at 60°C under dynamic vacuum for another 24 hr to yield COF-Pors.

Structural modeling

Structural modeling of COF-Pors (Figure S1) was determined under density functional theory (DFT) method using the DMol 3 program package in Materials Studio2018. The exchange and correlation terms were determined using the Generalized Gradient Approximation (GGA) in the form proposed by Perdew, Burke, and Ernzerhof (PBE). 10 cycles were set for the cell optimization with a displacement value 0.015Å. P1 symmetry was applied for the system. The hirshfeld charge analysis of the optimized structure was carried out. Subsequently, the COF material model containing 3 × 3 × 4 COF unit cells was designed and optimized under the COMPASS II force field in Forcite module.

ADDITIONAL RESOURCES

Additional resources containing the structural modeling images, FT-IR, NMR, XPS spectra, porosity analysis, stability test, EPR spectra, TEM images, SEM images, TA spectra, and NLO data can be found in the Supplemental Figures and Table file.